Transformation-induced plasticity in omega titanium

Cite as: J. Appl. Phys. **129**, 015105 (2021); https://doi.org/10.1063/5.0035465
Submitted: 28 October 2020 . Accepted: 15 December 2020 . Published Online: 06 January 2021

Amir Hassan Zahiri, Jamie Ombogo, Tengfei Ma, Pranay Chakraborty, and Lei Cao

Journal of Applied Physics ARTICLE scitation.org/journal/jap

Transformation-induced plasticity in omega titanium

Cite as: J. Appl. Phys. **129**, 015105 (2021); doi: 10.1063/5.0035465
Submitted: 28 October 2020 · Accepted: 15 December 2020 ·
Published Online: 6 January 2021

Amir Hassan Zahiri, Jamie Ombogo, Tengfei Ma, Pranay Chakraborty, and Lei Cao[a)]

AFFILIATIONS

Department of Mechanical Engineering, University of Nevada, Reno, Reno, Nevada 89557, USA

[a)]**Author to whom correspondence should be addressed:** leicao@unr.edu

ABSTRACT

ω-titanium (Ti) is a high-pressure phase that is conventionally perceived to be brittle and nondeformable, although direct investigations of its deformation process remain scarce. In this work, we perform molecular dynamics simulations to study the deformation process of ω-Ti with initial defects and find that stress-induced $\omega \rightarrow \alpha$ martensitic transformation can cause extensive plasticity in ω-Ti under various loading directions. Moreover, for the first time, we demonstrate that four types of transformation twins—$\{11\bar{2}1\}$, $\{11\bar{2}2\}$, $\{10\bar{1}2\}$, and $\{10\bar{1}1\}$ twins—can be formed through the $\omega \rightarrow \alpha$ martensitic phase transformation. This work advances the understanding of plastic deformation in ω-Ti and unveils the essential role of the metastable ω-phase in the formation of transformation twins.

I. INTRODUCTION

Extensive research efforts have been devoted to titanium (Ti) and its alloys due to their high strength-to-weight ratio and extraordinary high-temperature performance.[1–3] At ambient conditions, Ti prefers to exist in the hexagonal close-packed (hcp or α) phase, while it can transform into the ω-phase at high pressures or into the body-centered cubic (bcc or β) phase at high temperatures (around 1100 K). The ω-phase can be obtained under high pressure or shock loading experiments because the high pressure can modify the electronic band structure and stabilize the ω-phase.[4] In addition, alloying with d-rich transition metal elements, such as vanadium and niobium, can also stabilize the ω-phase.[4]

Since its discovery in 1954,[5] the ω-phase has received extensive interest because of its profound effect on the mechanical properties of Ti alloys.[6,7] The ω-phase has an $A1B_2$ structure and contains three atoms in the primitive unit cell, with one atom in the A-plane and two atoms in the B-plane. In particular, the A- and B-planes have different bonding properties: A-planes are purely metallic, like hcp and bcc Ti, while B-planes have certain covalent nature.[4] These peculiar properties were believed to cause the brittleness of the ω-phase. Thus, the ω-phase is commonly used as a precipitation-hardening mechanism to enhance the strength and microhardness of Ti alloys, though a large number of the ω precipitates can deteriorate the ductility of the alloys.[8,9]

Studies directly investigating the physical properties of the ω-phase are scarce[7,10,11] because the ω-phase usually exists as nano-sized precipitates in Ti alloys and was only recently obtained in the bulk form.[12] In 2013, Tane *et al.* investigated the elastic properties of ω-Ti produced by high-pressure torsion.[10] They found that ω-Ti has higher Young's modulus and shear modulus than the β- and α-phases, though the plastic deformation in the ω-phase remained unexplored. As an attempt to investigate the plastic deformation, Kumar *et al.* calculated the generalized stacking fault energy surfaces using the density-functional theory, through which they identified the favored slip modes in ω-Ti as prismatic $\langle c \rangle$, prismatic-II $[10\bar{1}0]$, and pyramidal-II $\langle c + a \rangle$.[7] Their density-functional theory calculation quantifies the relative ease of different slip systems, though methods that can handle millions of atoms are still required to study the dynamic process of plastic deformation. Accordingly, Zong *et al.* performed large-scale molecular dynamics (MD) simulations in single-crystal ω-Ti and found a highly anisotropic deformation behavior.[11] They observed that the superplastic deformation behavior was due to $\omega \rightarrow \alpha$ martensitic phase transformation under $[10\bar{1}0]$ compression as well as brittle fracture under [0001] loading. Nonetheless, only the pristine single crystal was studied, although Ti and its alloys, particularly the ω-Ti,[12,13] almost always contain considerable initial defects. As demonstrated by our previous work,[14–18] initial defects can affect the deformation process and mechanical properties of metals significantly. In this work, we

strive to systematically investigate the deformation process of quenched ω-Ti with initial defects owing to the omnipresence of ω-Ti in quenched metastable Ti alloys.

Ti and its alloys are well known to form transformation twins as a result of the martensitic phase transformation induced by quenching or mechanical strain.[19–22] Notably, $\{10\bar{1}1\}$ transformation twins were widely reported to form during $\beta \rightarrow \alpha$ martensitic phase transformation among a wide range of Ti alloys and pure Ti.[19–21] Similarly, the metastable ω-phase can transform back to the thermodynamically stable α-phase upon release of the high pressure or heating to around 150 °C and thus may also form transformation twins. For instance, the $\{10\bar{1}1\}$ twin was observed to form as a result of $\omega \rightarrow \alpha$ martensitic phase transformation in pure Ti.[11] Accordingly, the objective of this work is to rigorously investigate the deformation of ω-Ti with initial defects under various loading directions and to elucidate the formation mechanism of different transformation twins.

The rest of this paper is organized as follows: Sec. II describes the methodology of this work and the construction of the quenched ω-Ti structure. In Sec. III, we present our findings of the transformation-induced plasticity in ω-Ti and the formation mechanisms of transformation twins. Finally, we conclude this paper in Sec. V.

II. METHODOLOGY

A. MD simulations

In this work, we use the LAMMPS package[23] to perform all the MD simulations with a time step size of 1 fs. The interactions between Ti atoms are modeled by the embedded-atom method potential developed by Mendelev *et al.*[24] The initial simulation domain is α-Ti of $29.5 \times 25.5 \times 24.1\,\text{nm}^3$ (1×10^6 atoms) with the periodic boundary condition applied to all three dimensions. At the beginning of the simulation, we assign random atomic velocities following the Gaussian distribution with an average temperature of 10 K. In order to reduce the simulation time required for the melting process and to ensure the full melting of the Ti structure, we heat the structure to a temperature (2266 K) higher than the melting point (1923 K). To achieve complete melting, the simulation domain is maintained at 2266 K for 500 ps before it is quenched to 10 K. Subsequently, we relax the structure at 10 K and 0 Pa in the isothermal–isobaric ensemble using the Nosé–Hoover thermostat[25] and the Parrinello–Rahman barostat[26] for 100 ps. The ω-phase is predicted by the adopted Mendelev *et al.*'s[24] interatomic potential to only have a slightly higher energy (7 meV/atom) than the α-phase. As a result, the quenching simulation generates an ω-Ti structure, which is stabilized by the fast quenching rate and the abundant internal defects. To study the deformation process, we apply uniaxial loading to the quenched ω-Ti structure with a strain rate of $10^8\,\text{s}^{-1}$. It should be noted that the application of a very high strain rate even in the order of $10^{11}\,\text{s}^{-1}$ in MD simulations is very common.[27–30] Despite the high strain rate, previous MD simulations have provided useful guidance or rigorous interpretations to deformation behaviors under realistic conditions. We applied uniaxial loading by changing the simulation box length in the loading direction at a constant strain rate and then remapping the atom coordinates within the modified simulation box. As a result of Poisson's effect, the changes of the other two boundaries are naturally incorporated by solving the isothermal–isobaric equations of motion at zero pressure. OVITO[31] is used to visualize and analyze the microstructure evolution. Common neighbor analysis[32,33] is used to identify the crystal structure, with ω, β, α, and face-centered cubic (fcc) phases denoted in yellow, red, cyan, and green, respectively.

B. Lattice dynamics calculations

In our lattice dynamics calculations, supercells of α ($5 \times 5 \times 5$), ω ($3 \times 3 \times 3$), and β ($4 \times 4 \times 4$) are fully relaxed at zero pressure. The raw second-order force constants are obtained using the central finite difference method and are further adjusted with the linear regression approach (ordinary least squares) to apply the symmetry constraints.[37] Afterward, the symmetrized force constants are used to calculate the dynamical matrix from which we obtain the phonon bandstructure (the phonon eigenvectors and eigenvalues). To ensure the direct correspondence between our lattice dynamics calculations and MD simulations, we use the same cutoff radius and empirical interatomic potential in these two types of calculations/simulations.

III. RESULTS

First, we will describe the deformation process of the ω-Ti structure under six loading conditions. Then, we will analyze the formation mechanisms for each of the five transformation twins observed in our MD simulations. Finally, we will discuss the orientation relations of all the α-variants captured by our MD simulations.

A. The radial distribution functions

As shown in Fig. 1(a), the quenched Ti structure contains some retained β-phase and traces of the α-phase. More specifically, common neighbor analysis reveals that it has 11.8% of the β-phase and 2.4% of the α-phase initially. It is composed of a predominant grain and a much smaller grain, which is close to a single-crystal ω-Ti. Its ω-phase nature is further confirmed by the radial distribution function (RDF) in Fig. 1(b), in which the RDF of the quenched structure displays similar peaks as those of the single-crystal ω-phase. Notably, the first three peaks in RDFs (2.675, 2.825, and 3.025 Å) correspond to the first three nearest neighbors in the ω-phase that are highlighted in the inset of Fig. 1(b). We study six loading conditions, in each case, the uniaxial tension or compression is applied along the x-, y-, or z-axis of the simulation domain. The orientation of the initial ω-Ti structure with respect to x-, y-, and z-axes is shown in Fig. 1(c). Figure 2 shows the evolution of the RDFs under all six loading conditions, from which we observe the gradual change in the RDF from that of the ω-phase to that of the α-phase. Specifically, with increasing strain, the peaks belonging to the ω-phase broaden owing to the elastic strain and the activation of $\omega \rightarrow \alpha$ martensitic phase transformation. As a result, the second and third peaks merge into one broad peak when the strain reaches 5%. With an increasing amount of the α-phase, the most prominent peak in the RDF gradually shifts from 3.025 Å of the ω-phase to 2.92 Å of the α-phase. The former

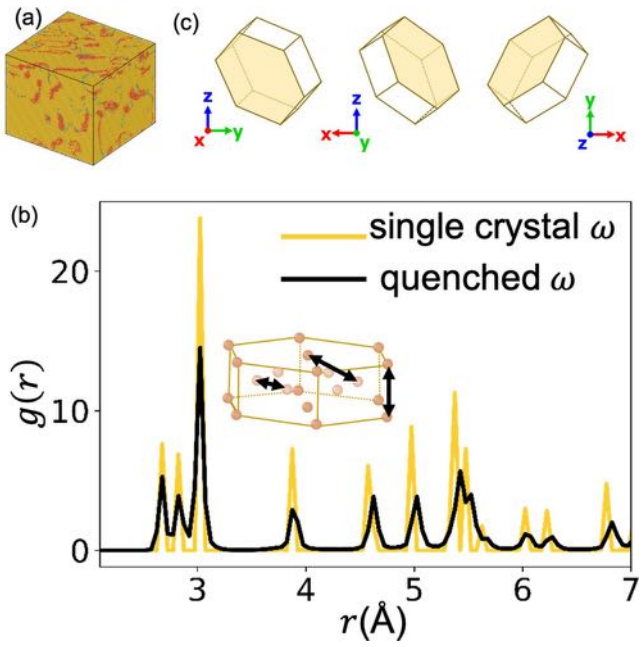

FIG. 1. (a) The quenched ω-Ti structure and (c) its orientation with respect to x-, y-, and z-axes. The basal plane of the ω unit cell is highlighted in yellow. (b) The comparison of the RDF between the quenched ω-Ti structure and single crystal ω-Ti. The first three peaks of the RDF correspond to the first three nearest neighbors in the ω-phase, of which the atom pairs are connected by the black arrows in the inset.

is the distance between atoms in the A-plane and atoms in the B-plane of the $A1B_2$ structure of the ω-phase, while the latter is the distance between two atoms in the basal plane of the α-phase. Notably, the first peak corresponding to the nearest-neighbor distance of 2.675 Å in the ω-phase completely disappears at 20% strain under x-axis compression [Fig. 2(a)], y-axis compression [Fig. 2(c)], and z-axis tension [Fig. 2(f)], suggesting the transformation of almost all the parent ω-phase.

B. The stress–strain curves

To further investigate the phase transformation and plastic deformation quantitatively, we plot the evolution of the percentages of ω-Ti and α-Ti and the stress–strain curves in Fig. 3. The β-phase shows a continuous decreasing trend and a small percentage ($< 3\%$) and is thus omitted in Fig. 3. During the elastic regime, we observe a slight increase in the percentage of the ω-phase and a stable small percentage of the α-phase. The former is due to the transformation from the β-phase that is retained from the quenching process. Upon yielding, the $\omega \rightarrow \alpha$ martensitic phase transformation is activated, leading to the most prominent stress drops in the stress–strain curves. The $\omega \rightarrow \alpha$ phase transformation proceeds with increasing applied strain, and, thus, the percentage of ω-Ti keeps decreasing, while that of the α-Ti keeps increasing. In addition, because our initial ω-Ti structure contains defects, the propagating ω–α interfaces can decelerate when they are impeded by the defects and then accelerate again after they bypass the defects. The accelerated ω–α interfaces account for some of the smaller stress drops in the stress–strain curves.

Our MD simulations reveal that the $\omega \rightarrow \alpha$ phase transformation displays different kinetics under different loading directions. Specifically, the phase transformation occurs quickly under x-axis compression [Fig. 3(a)], y-axis compression [Fig. 3(c)] and tension [Fig. 3(d)], and z-axis tension [Fig. 3(f)], leading to a high percentage of Ti in the form of α-phase (>70%) and a low percentage in the ω-phase ($< 25\%$) at the end of the deformation process. In contrast, the phase transformation occurs at a lower speed under x-axis tension [Fig. 3(b)] and z-axis compression [Fig. 3(e)], and the final percentages of Ti in the α-phase are only around 50%. This difference can be clearly seen from the microstructures at 10% and 20% strains in the insets of Fig. 3. It should be noted that the ω-phase is identified as amorphous atoms by common neighbor analysis, and thus, the percentage shown in Fig. 3 accounts for both ω-phase and amorphous atoms. A careful examination of the microstructures reveals that amorphous atoms mostly form at the end of the $\omega \rightarrow \alpha$ phase transformation and are much fewer than the actual ω-phase atoms because they mainly exist in dislocations and twin boundaries in the newly formed α-variant.

C. The martensite microstructure

The $\omega \rightarrow \alpha$ phase transformation leads to complex martensite microstructure, including five types of transformation twins. Specifically, we observe $\{11\bar{2}1\}$ twins [Fig. 4(a)] and $\{10\bar{1}2\}$ twins [Fig. 4(b)] under x-axis compression, $\{11\bar{2}2\}$ twins under y-axis tension [Fig. 4(c)], $\{10\bar{1}1\}$ twins under x-axis tension [Fig. 4(d)], and threefold twins under the z-axis tension [Fig. 4(e)]. In the threefold twin, three cozone $\{10\bar{1}1\}$ twin boundaries join at a common $\langle 11\bar{2}0\rangle_\alpha$ axis, as shown in Fig. 4(e). Our simulations under y-axis compression and z-axis compression only reveal a single newly formed α-phase.

Previously, only $\{10\bar{1}1\}$ twins were identified as transformation twins in pure Ti, which is caused by temperature-induced $\beta \rightarrow \alpha$ phase transformation[19] or stress-induced $\omega \rightarrow \alpha$ phase transformation.[11] In this work, we have shown, for the first time, that $\{11\bar{2}1\}$, $\{11\bar{2}2\}$, and $\{10\bar{1}2\}$ twins, as well as the threefold $\{10\bar{1}1\}$ twins, can all be formed through stress-induced $\omega \rightarrow \alpha$ martensitic phase transformation in pure Ti. To rule out the empirical potential dependence of our results, the MD simulation of x-axis compression has been performed using a modified embedded-atom method potential for Ti,[34] which is carefully designed to capture the $\alpha \leftrightarrow \omega$ martensitic phase transformation. The MD simulation using the second potential also predicts the formation of $\{11\bar{2}1\}$ twins [Fig. 4(f)] and $\{10\bar{1}2\}$ twins under x-axis compression, reaffirming our findings.

D. The formation mechanism of various transformation twins

The core of this section is to demonstrate that the aforediscussed dependence of twinning mode on the loading directions is rooted in different orientation relation of $\omega \rightarrow \alpha$ martensitic phase transformation. Specifically, we observe two different

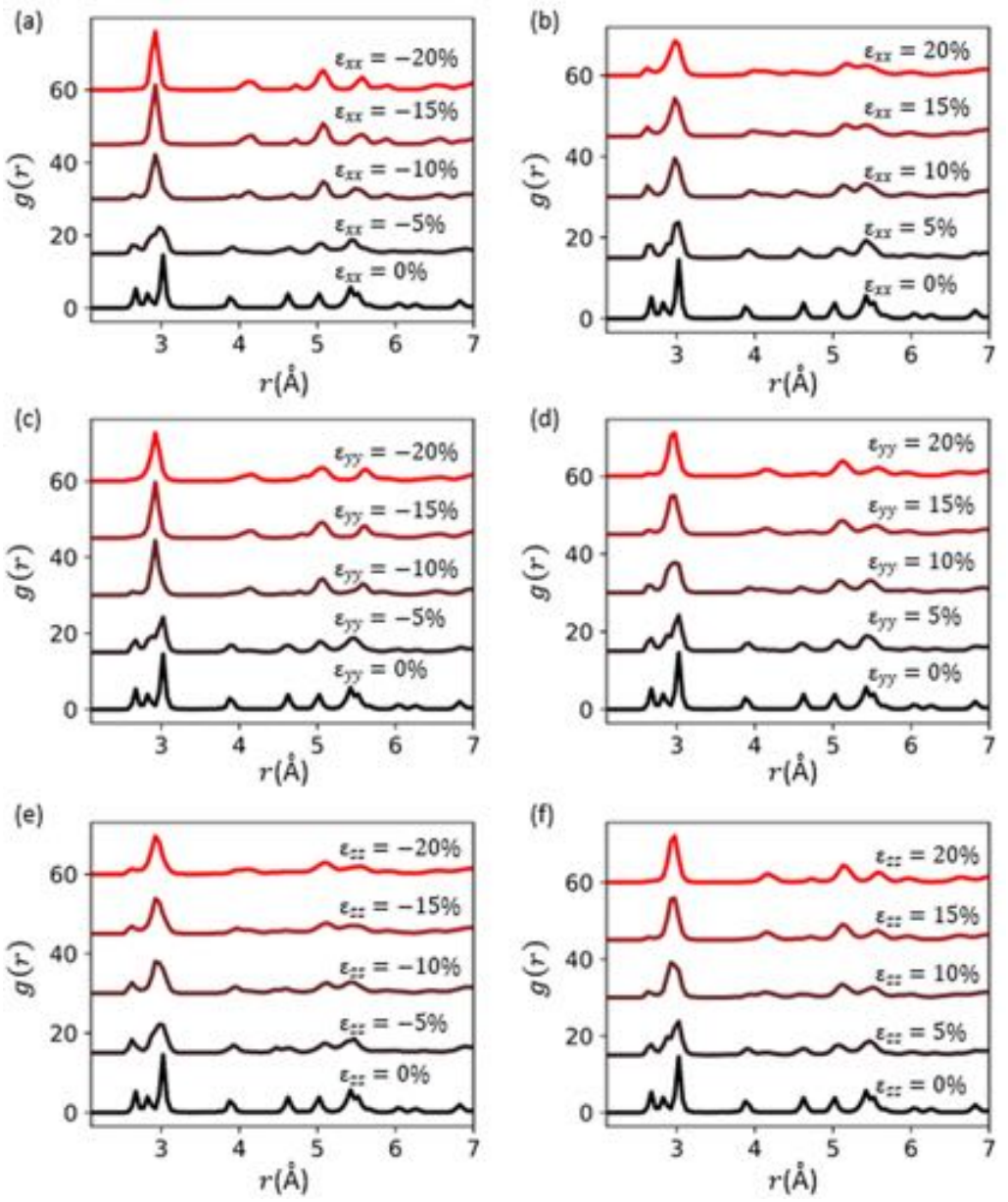

FIG. 2. The evolution of RDFs during the deformation process under (a) x-axis compression, (b) x-axis tension, (c) y-axis compression, (d) y-axis tension, (e) z-axis compression, and (f) z-axis tension.

orientation relations in our MD simulations, in which the correspondence of ω- and α-phases will be discussed in more details in Sec. IV B. The two orientation relations are the same as Variant I and Variant II in Usikov and Zilbershtein's notation[35] and are referred to as OR I and OR II in this paper to avoid any confusion with variant of martensite. Specifically, in OR I, $(0001)_\alpha \parallel (01\bar{1}1)_\omega$ and $[11\bar{2}0]_\alpha \parallel [\bar{1}011]_\omega$; in OR II, $(0001)_\alpha \parallel (11\bar{2}0)_\omega$ and $[11\bar{2}0]_\alpha \parallel [0001]_\omega$.

As displayed in Fig. 5, the parent ω-phase can transform into two α-variants through two separate OR I or mixed OR I and OR II. As a result, different twins are formed owing to the different misorientation angles between the two newly formed α-variants. As schematically shown in Fig. 5(a), two separate OR I—two crystallographically equivalent $\{01\bar{1}1\}_\omega$ planes of the parent ω-phase directly transform into the basal planes of two α-variants—can form a $\{11\bar{2}2\}_\alpha$ twin. Because these two $\{01\bar{1}1\}_\omega$ planes share a common

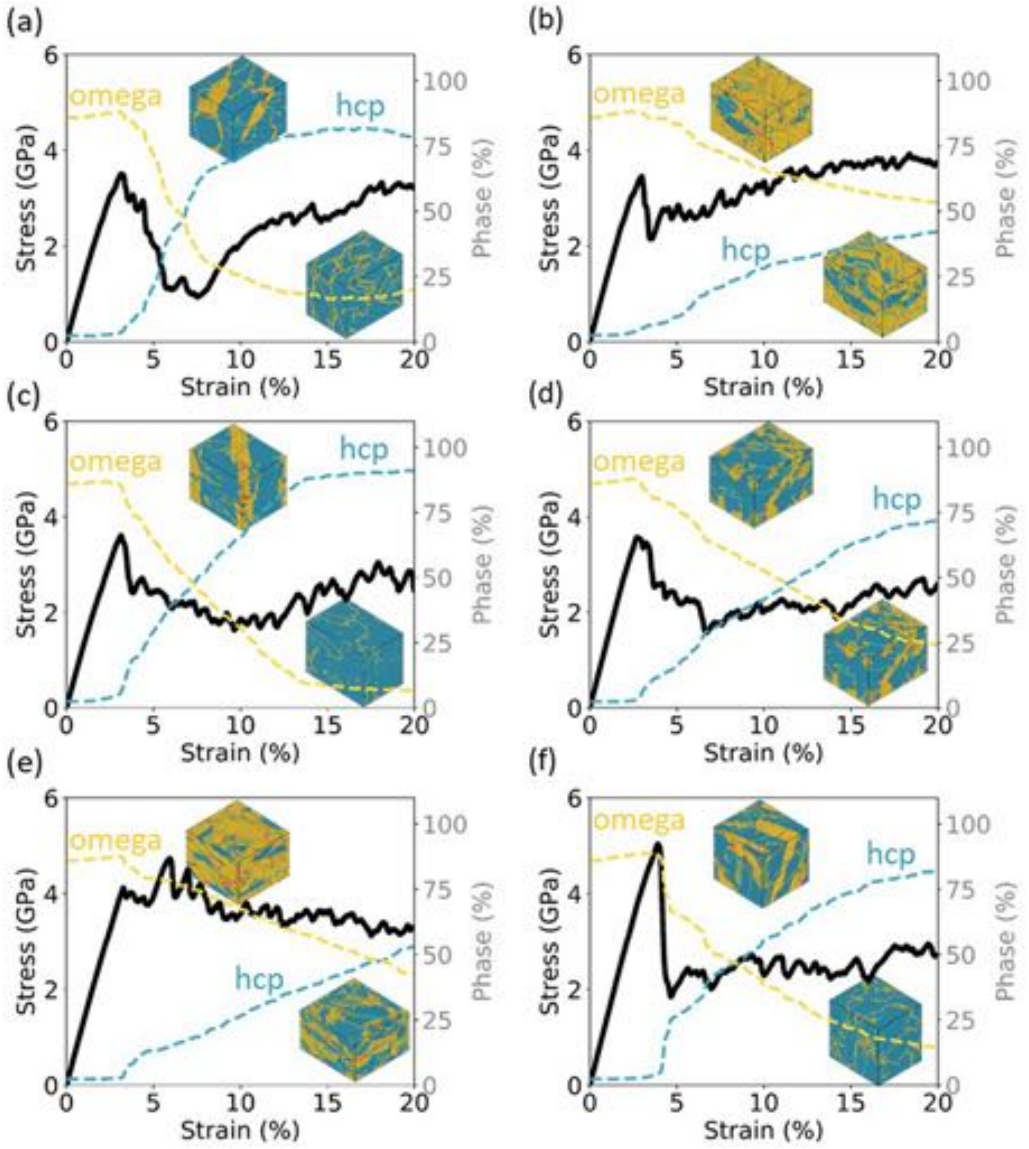

FIG. 3. The stress–strain curves (black lines) and the percentage of ω-Ti (yellow dashed lines) and α-Ti (cyan dashed lines) under (a) x-axis compression, (b) x-axis tension, (c) y-axis compression, (d) y-axis tension, (e) z-axis compression, and (f) z-axis tension. The insets show the corresponding microstructures at 10% and 20% applied strains.

$\langle 11\bar{2}0\rangle_\omega$ direction, this process can be clearly demonstrated by the projection of our MD simulation along the common $\langle 11\bar{2}0\rangle_\omega$ direction, as shown in Fig. 5(b). Under y-axis tension, the left and right regions of the same ω-phase transform into two different α-variants. Upon the merging of the two α-variants, a coherent twin boundary forms in between. The twin boundary shows a misorientation angle of 65° and a three-atom interface structure, matching those of the $\{11\bar{2}2\}$ twin boundary in α-Ti. It should be noted that this twin formation process is possible because the angle between the two $\{01\bar{1}1\}_\omega$ planes (63°) is very close to the misorientation angle of the $\{11\bar{2}2\}$ twin (65°).

Similarly, two separate OR I can form a $\{11\bar{2}1\}$ twin, as schematically shown in Fig. 5(c). In this case, the two $\{01\bar{1}1\}_\omega$ planes share a common $\langle 11\bar{2}3\rangle_\omega$ direction, which differs from the above case of $\{11\bar{2}2\}$ twin. Figure 5(d) shows the detailed formation process of the $\{11\bar{2}1\}$ twin in our MD simulation of x-axis compression. The right region of the parent ω-phase transforms into the first α-variant. Subsequently, the second α-variant nucleates at the ω–α interface and continues to consume the parent ω-phase, forming a twin boundary with respect to the first α-variant. Obviously, the misorientation of 33° and the alternate three-atom/two-atom interface structure match those of the $\{11\bar{2}1\}$ twin

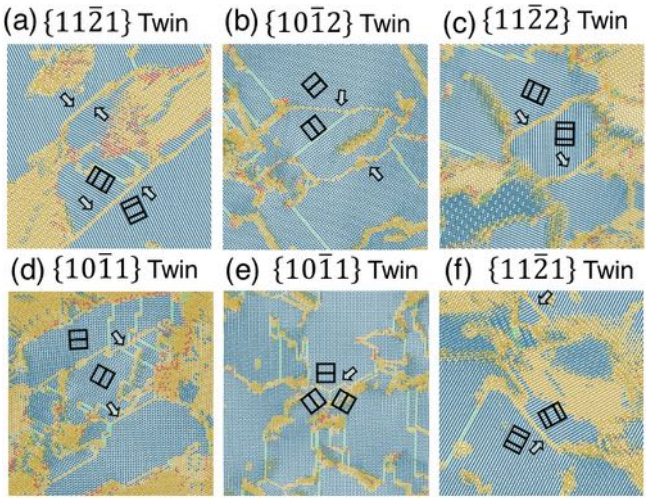

FIG. 4. Slices of the martensite microstructures clearly showing five types of transformation twins formed in our MD simulations under (a) and (b) x-axis compression, (c) y-axis tension, (d) x-axis tension, and (e) z-axis tension. (f) The simulation of x-axis compression has been verified using another modified embedded atom method potential for Ti,[34] which also shows the formation of {11$\bar{2}$1} twins.

boundary in α-Ti. Similar to the {11$\bar{2}$2} twin, the formation of the {11$\bar{2}$1} twin is made possible by the matching between the misorientation angles of the {11$\bar{2}$1} twin and the two $\{01\bar{1}1\}_\omega$ planes involved, as listed in Table I.

In contrast to the aforementioned two types of twins formed through two separate OR I, the {10$\bar{1}$2} twin is formed through the simultaneous occurrence of OR I and OR II, as schematically shown in Fig. 5(e). Figure 5(f) shows our MD simulation of x-axis compression projected along the $\langle 11\bar{2}0\rangle_\omega$ direction. Evidently, the ω–α interface on the right side contains a thin layer of β-phase and follows OR I, while the left ω–α interface follows OR II. The merging of the two newly-formed α-variants results in a coherent {10$\bar{1}$2} twin boundary.

In a different case, the simultaneous occurrence of OR I and OR II can lead to the formation of a {10$\bar{1}$1} twin, as schematically shown in Fig. 5(g). Our MD simulation of x-axis tension is projected along the $\langle\bar{1}011\rangle_\omega$ direction in Fig. 5(h), in which the merging of the two α-variants leads to a coherent {10$\bar{1}$1} twin boundary.

Finally, we note that the simultaneous occurrence of two separate OR I and one OR II can lead to the formation of a threefold {10$\bar{1}$1} twin, as illustrated in Fig. 5(i). Our MD simulation of z-axis tension is projected along the $\langle\bar{1}011\rangle_\omega$ direction in Fig. 5(h), which captures the formation of three cozone {10$\bar{1}$1} twin boundaries adjoining at a common $\langle 11\bar{2}0\rangle_\alpha$ axis. Compared to a single {10$\bar{1}$1} twin, the threefold {10$\bar{1}$1} twin can better accommodate the strain associated with the martensitic phase transformation. Similar threefold symmetry has been observed in the martensite microstructure of pure Ti,[22] Ti alloy,[21] iron,[36] and Ni-Al alloys.[37]

E. The crystallographic origin of the twin formation process

We note that the formation of all the transformation twins is rooted in the fact that the angles between the crystallographic planes in the ω-phase ($\{01\bar{1}1\}_\omega$ and/or $\{11\bar{2}0\}_\omega$)—which can directly transform into the basal planes of the α-variants—are close to the misorientation angles of the twins. The relevant values are summarized in Table I.

Furthermore, we emphasize that the α-variants—that constitute the five types of transformation twins are not completely independent—as they can be involved in more than one type of twins. As shown in Fig. 5, the planes highlighted in purple are involved in multiple twins, so are the planes highlighted in dark green and light blue. Theoretically, there are six $\{01\bar{1}1\}_\omega$ planes and three $\{11\bar{2}0\}_\omega$ planes in the parent ω-phase. The direct transformation of these planes to basal planes of the α-variants can lead to the formation of a maximum of nine α-variants. Under the six loading directions applied in our MD simulations, we observed seven of them ($\alpha1$–$\alpha7$). Of these, the basal planes come from five $\{01\bar{1}1\}_\omega$ planes and two $\{11\bar{2}0\}_\omega$ planes of the parent ω-phase. As shown in Fig. 6, $\alpha1$ and $\alpha2$ form the $\{11\bar{2}2\}_\alpha$ twin; $\alpha1$ and $\alpha3$ form the $\{11\bar{2}1\}_\alpha$ twin; $\alpha1$ and $\alpha4$ form the $\{10\bar{1}2\}_\alpha$ twin; $\alpha4$, $\alpha5$, and $\alpha6$ form the threefold $\{10\bar{1}1\}_\alpha$ twin; and $\alpha5$ and $\alpha7$ form the $\{10\bar{1}1\}_\alpha$ twin.

F. Potential energy evolution

Besides the above crystallographic analysis of the twin formation process, we further examine the evolution of the potential energy for four types of transformation twins. Regions of approximately 400 atoms around the transformation twins are traced and their potential energy evolution is shown in Fig. 7. Additionally, the microstructure at the instants of large energy change is included as the inset in Fig. 7. In all four cases, the potential energy shows two sharp increases—corresponding to the sequential formation of two α-variants—before reaching the peak. Subsequently, the consumption of the parent ω-phase by the α-variants leads to moderate drops in the potential energy because the α-phase has lower cohesive energy than the ω-phase in the embedded-atom method potential ($\Delta E = 7$ meV/atom). Larger drops in the potential energy are observed for the formation of twin boundaries. Finally, the coherent twin boundaries have a slightly lower potential energy than that in the initial ω-phase.

During this process, there are two competing factors that cause the potential energy to initially increase and then decrease. The first one is a bulk contribution from the energy difference between the α- and ω-phases ($\Delta E = 7$ meV/atom in the embedded-atom method potential). The second one is an interfacial contribution from the excess energy of the amorphous and β atoms in the α-ω interfaces. Notably, the interfacial contribution dominates at the beginning and thus the potential energy keeps increasing because the β-phase has an excess energy ($\Delta E_{hcp-bcc} = 74$ meV/atom) one order of magnitude higher than that of the ω-phase ($\Delta E_{hcp-\omega} = 7$ meV/atom). After reaching the peak, the bulk contribution dominates due to the large amount of transformed atoms, leading to a moderate energy drop. The most prominent energy drop comes from the formation of twin boundaries, which replaces the α-ω interfaces and eliminates the

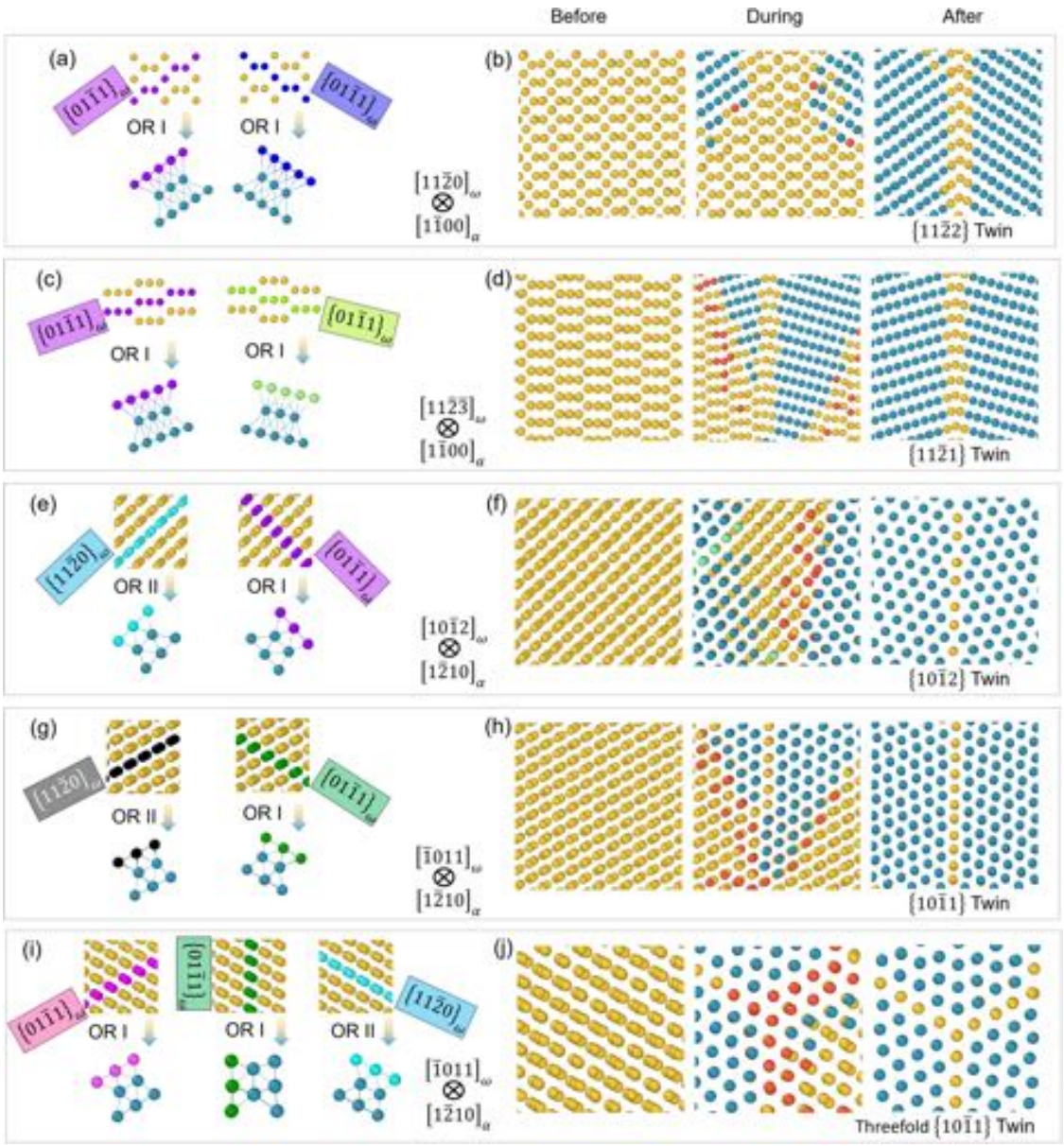

FIG. 5. The formation processes of the five transformation twins in our MD simulations are shown in (b), (d), (f), (h), and (j), while (a), (c), (e), (g), and (i) are the corresponding schematics. The plane correspondence during the $\omega \rightarrow \alpha$ phase transformation is demonstrated by the highlighting colors. The planes that are highlighted by the same color among different cases are the same plane in the parent ω-phase. The purple, blue, green, dark green, and pink planes are $\{01\bar{1}1\}_\omega$ planes; the light blue and black planes are $\{11\bar{2}0\}_\omega$ planes.

interfacial contribution. In particular, the formation of twin boundaries are associated with the abrupt energy drops at 476 ps in Fig. 7(a), at 180 ps in Fig. 7(b), at 328 ps in Fig. 7(c), and at 520 ps in Fig. 7(d). In addition, smaller energy drops are identified to correspond to dislocations slip in the ω-phase—at 152 ps in Fig. 7(b)—and in the α-phase—at 308 ps in Fig. 7(d).

IV. DISCUSSIONS

A. The role of initial defects

As discussed in Sec. III B, our MD simulations reveal significant phase transformation-induced plasticity in ω-Ti without brittle fracture under all the loading directions. We note that

TABLE I. The misorientation angles of each transformation twin and the angles between ω planes involved in the twin formation process. The latter is taken as an acute angle to be consistent with the definition of the former. * Calculation based on $c/a = 0.613$ for ω-Ti.

Twin type	$\{11\bar{2}2\}$	$\{11\bar{2}1\}$	$\{10\bar{1}2\}$	$\{10\bar{1}1\}$
Theoretical misorientation angle	65°	35°	85°	57°
Misorientation angle measured in MD	65 ± 1°	33 ± 1°	87 ± 1°	60 ± 1°
The angle between participating ω planes*	63°	32°	90°	60°

previous studies mostly reported ω-phase as a brittle phase.[6,38,39] This is not in conflict with our work. In fact, the ω-phase studied in those studies was rather stable due to alloying with niobium or other elements, which does not transform into α-phase upon deformation. In contrast, the plasticity (or ductility) observed in our MD simulations on quenched pure Ti is caused by ω-to-α phase transformation, instead of the ω-phase itself. Furthermore, we note that the extensive phase transformations in quenched pure Ti are not surprising. First, the ω-phase has a slightly higher (by 7 meV/atom) energy than the α-phases; as a comparison, the β-phase is 110 meV/atom higher in energy than the α-phase. Accordingly, the elastic strain energy caused by external loading can well activate ω-to-α phase transformations. Second, our Ti structure contains plenty of defects that assist the activation of ω-to-α phase transformation to accommodate the plastic deformation, as discussed next.

It is well known that the rate-limiting step of martensitic phase transformation is the initial nucleation, which usually starts from material defects.[40] Therefore, the high transformation-induced plasticity observed is attributed to the initial defects in the quenched ω-Ti structure that serve as martensite embryos, facilitating the nucleation step of the stress-induced martensitic phase transformation. To confirm the role of initial defects, we simulate the deformation of a pristine single crystal ω-Ti with a similar domain size ($27.6 \times 25.89 \times 22.56\,\text{nm}^3$) as the quenched ω-Ti structure. As shown in Table II, the percentage of the α-martensite in the former is much lower than that in the latter. Specifically, at a strain of 0.2, the pristine single crystal only contains $\leq 15\%$ α-phase under four loading directions. In contrast, the quenched Ti contains mostly α-phase under four loading directions and ~50% α-phase in the other two loading directions.

B. The mechanism of $\omega \rightarrow \alpha$ phase transformation

Because of the metastable nature of the ω-phase, $\omega \rightarrow \alpha$ phase transformation has rarely been studied, though its reverse process—$\alpha \rightarrow \omega$ phase transformation—has been investigated by both experiments and atomistic simulations.[35,41–49] Specifically, two orientation relations have been established for $\alpha \rightarrow \omega$ martensitic phase transformation, commonly referred to as Variant I (OR I) and Variant II (OR II) following Usikov and Zilbershtein's notation:[35]

$$\text{OR I: } (0001)_\alpha \parallel (01\bar{1}1)_\omega, \quad [11\bar{2}0]_\alpha \parallel [\bar{1}011]_\omega, \tag{1}$$

$$\text{OR II: } (0001)_\alpha \parallel (11\bar{2}0)_\omega, \quad [11\bar{2}0]_\alpha \parallel [0001]_\omega. \tag{2}$$

Usikov and Zilbershtein calculated the orientation relation of $\alpha \rightarrow \omega$ phase transformation using the well-known correspondence matrices of $\alpha \rightarrow \beta$ and $\beta \rightarrow \omega$ phase transformations and they obtained two crystallographically nonequivalent orientation relations. Their calculation involves an intermediate β-phase and is regarded as an indirect transformation pathway, while direct ones—TAO-1[46] and Silcock[41] pathways—have also been developed for $\alpha \rightarrow \omega$ phase transformation. It should be noted that the

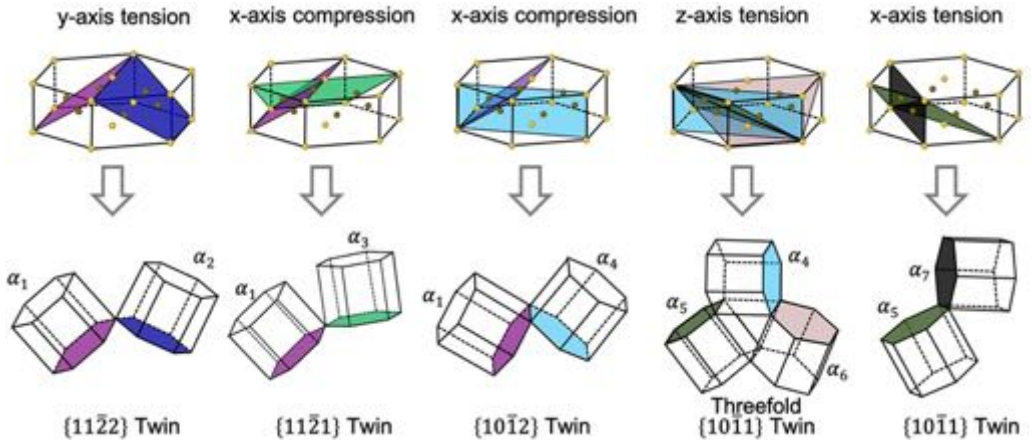

FIG. 6. Schematics showing the formation of seven α-variants ($\alpha 1$– $\alpha 7$) and five corresponding twins as a result of the $\omega \rightarrow \alpha$ martensitic phase transformation. In our MD simulations, two $\{11\bar{2}0\}_\omega$ planes (highlighted in light blue and black in the ω unit cells) and five different $\{01\bar{1}1\}_\omega$ planes (highlighted in purple, blue, green, pink, and dark green in the ω unit cells) directly transform into basal planes of $\alpha 1 \sim \alpha 7$. The same color scheme as in Fig. 5 is used to highlight the plane correspondence. The arrows represent the $\omega \rightarrow \alpha$ martensitic phase transformation.

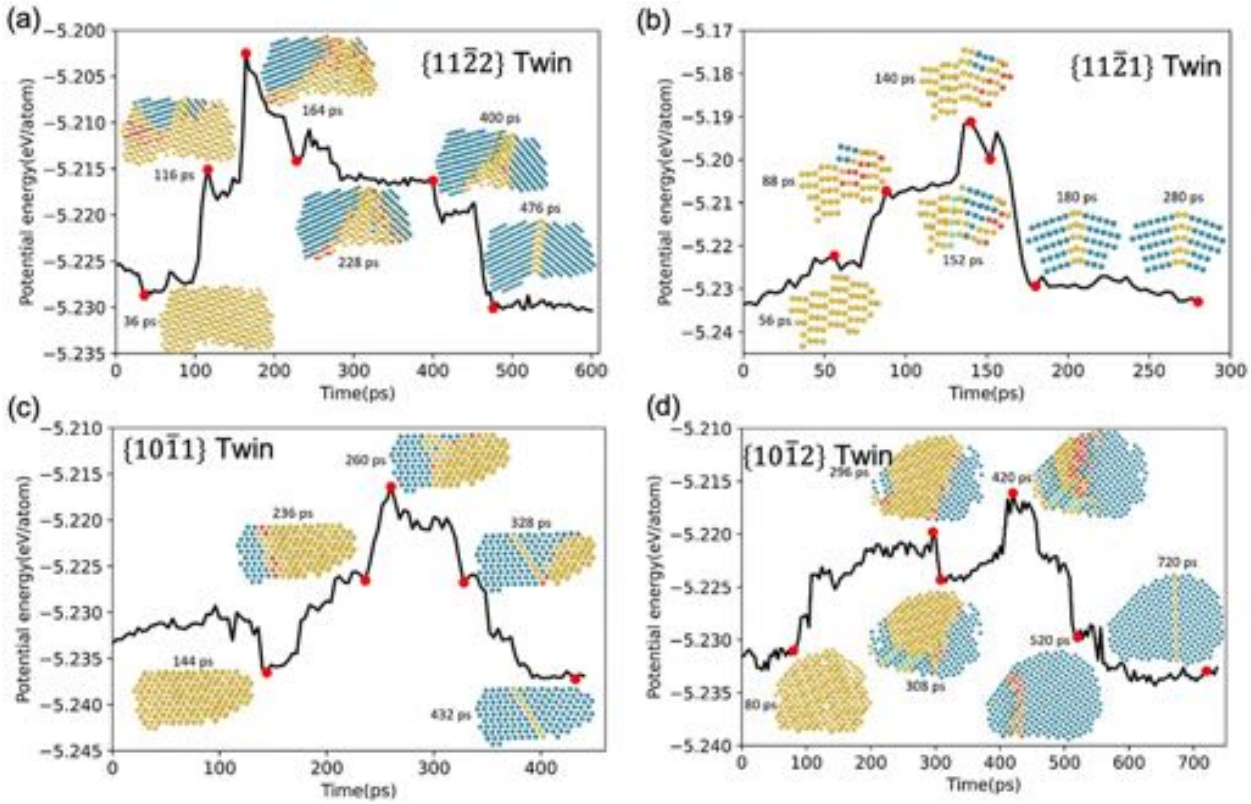

FIG. 7. The evolution of the average potential energy during the formation of four types of transformation twins. The microstructure at the instants of large potential energy change is included as the inset.

TAO-1 pathway conforms to OR I, while the Silcock pathway conforms to OR II. The TAO-1 pathway was found to have an energy barrier approximately a quarter of the Silcock pathway, although both orientation relations were observed experimentally.[35,41–45,47,49]

A careful examination of the $\omega \rightarrow \alpha$ phase transformation in our MD simulations reveals that it also follows either OR I or OR II for $\alpha \rightarrow \omega$ phase transformation. To demonstrate this, two groups of atoms are traced in our MD simulations and are shown in Fig. 8. In OR I [Fig. 8(a)], seven atoms in a corrugated $\{01\bar{1}1\}_\omega$ plane are highlighted by different colors: three black atoms from the top B-plane of the $A1B_2$ structure, one purple atom from the

TABLE II. The percentage of α-phase in the single-crystal ω-Ti at the strain of 0.2 and 0.3 under various loading directions. "T" and "C" represent tension and compression, respectively.

Loading type	[0001] T	[0001] C	[11$\bar{2}$0] T	[11$\bar{2}$0] C	[1$\bar{1}$00] T	[1$\bar{1}$00] C
0.2 strain	3.2%	50.4%	91.9%	10.1%	15.1%	10.8%
0.3 strain	5.3%	63.1%	91.1%	14.8%	50.9%	18.7%

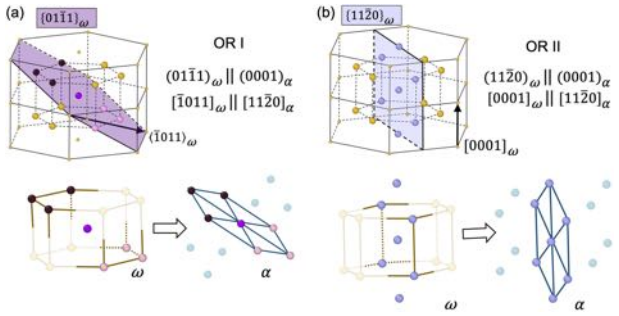

FIG. 8. Two groups of atoms are traced to demonstrate OR I (a) and OR II (b). (a) Top row: one $\{01\bar{1}1\}_\omega$ plane spanning over two ω-unit cells is highlighted in purple, in which the atoms traced during the phase transformation have a larger size. Bottom row: seven atoms in the corrugated $\{01\bar{1}1\}_\omega$ plane are highlighted by different colors; three black atoms from the top B-plane of the $A1B_2$ structure, one purple atom from the middle A-plane, three pink atoms from the bottom B-plane. These seven atoms form the basal plane of α-phase under the phase transformation. (b) Top row: one $\{11\bar{2}0\}_\omega$ plane spanning over two ω-unit cells is highlighted in light purple, in which the atoms traced during the phase transformation have a larger size. Bottom row: seven purple atoms in a $\{11\bar{2}0\}_\omega$ plane form the basal plane of α-phase after the phase transformation.

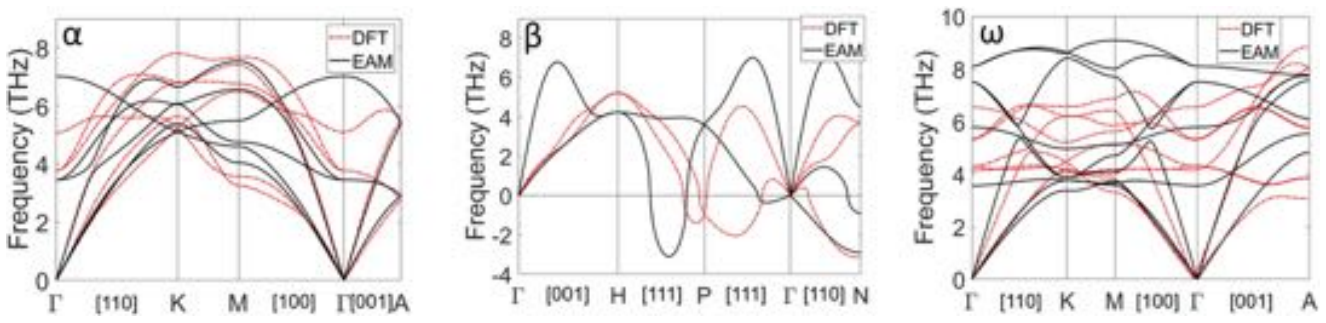

FIG. 9. The comparison between the phonon dispersion curves obtained from our lattice dynamics calculations (EAM) and those obtained from density-functional theory (DFT) calculations[34] for the three Ti phases, α, ω, and β.

middle A-plane, and three pink atoms from the bottom B-plane. After the phase transformation, these seven atoms form the basal plane of the α-phase: a regular hexagon around a central atom. In contrast, in OR II [Fig. 8(b)], seven purple atoms in the same $\{11\bar{2}0\}_\omega$ plane—four from the B-plane and three from A-plane—will form the basal plane of the α-phase. It should be noted that the $\omega \rightarrow \alpha$ phase transformation following OR I observed in our MD simulations always involves a thin layer of the β-phase at the ω–α interface, which can be considered as the signature of OR I.

C. The phonon dispersion relations

It is evident that the martensitic phase transformation between the ω-Ti and α-Ti plays a key role in the formation of transformation twins. To ensure that our MD simulation results reasonably reflect the realistic phase transformation process in Ti, we compare the detailed phonon band structure (i.e., dispersion relations) calculated from lattice dynamics (using the same embedded-atom method potential as that in our MD simulations) with that obtained from density-functional theory calculations.[34]

Figure 9 shows the phonon dispersion curves for the three Ti phases, α, ω, and β. Obviously, the phonon dispersion curves calculated using the embedded-atom method potential agree reasonably with those from density-functional theory calculations. Notably, the β-Ti has negative phonons around the N-point and the P-point, corresponding to the dynamic instabilities of the [110] transverse-acoustic phonon branch and $\frac{2}{3}$[111] longitudinal-acoustic phonon branch, respectively. The former causes the phase transformations from β- to α-Ti, while the latter causes the transformation from β- to ω-Ti. As a result, β-Ti is only stabilized by phonon entropy at high temperatures.[50]

For ω-Ti, the density-functional theory result shows stiffer phonon modes along the [001] branch than the basal plane directions ([100]) due to the c/a ratio of 0.613. In contrast, the phonon dispersion from embedded-atom method potential displays stiffer phonon modes for basal plane directions than those in the [001] branch, which is attributed to the larger c/a ratio of 0.637 in the embedded-atom method potential. This deviation would predict different elastic response of the ω-phase but should not adversely affect the twin formation process. This is further confirmed by that the same twin formation process is predicted by the modified embedded-atom method potential that successfully captures the stiffer [001] phonon,[34] as shown in Fig. 4(f).

V. CONCLUSIONS

In summary, our MD simulations demonstrated that ω-Ti can undergo significant plastic deformation owing to stress-induced $\omega \rightarrow \alpha$ martensitic phase transformation, assisted by the initial defects in the quenched ω-Ti structure. Moreover, we discovered that the stress-induced $\omega \rightarrow \alpha$ martensitic phase transformation can lead to the formation of four types of transformation twins in hcp Ti, $\{11\bar{2}1\}$, $\{11\bar{2}2\}$, $\{10\bar{1}2\}$, and $\{10\bar{1}1\}$ twins. We found that the type of the twins—which is defined by the misorientation angle between the two α-variants—is determined by the orientation relation of the $\omega \rightarrow \alpha$ martensitic phase transformation. Specifically, two separate OR I can form a $\{11\bar{2}1\}$ or a $\{11\bar{2}2\}$ twin, one OR I and one OR II can form a $\{10\bar{1}2\}$ or a $\{10\bar{1}1\}$ twin, and two separate OR I plus one OR II can form a threefold $\{10\bar{1}1\}$ twin. Our findings expand the type of transformation twins in hcp Ti from only $\{10\bar{1}1\}$ twin[11,19] to four different types and unveil the essential role of the metastable ω-phase in the formation of transformation twins. This work sheds light on the deformation process and mechanical properties of Ti alloys containing the ω-phase.

AUTHORS' CONTRIBUTIONS

A.H.Z. and J.O. contributed equally to this work. L.C. designed and directed the project. All authors discussed the results and contributed to the writing of the manuscript.

ACKNOWLEDGMENTS

The authors are partially supported by L.C.'s faculty startup funds from the University of Nevada, Reno. The authors acknowledge the partial financial support from the NSF-CBET TTP-Thermal Transport Process Program and the NSF EPSCoR Program (Grant No. 1953300). The authors also would like to acknowledge the support of Research & Innovation and the Office of Information Technology at the University of Nevada, Reno for

computing time on the Pronghorn High-Performance Computing Cluster.

DATA AVAILABILITY

The data that support the findings of this study are available from the corresponding author upon reasonable request.

REFERENCES

[1]I. J. Polmear, "Recent developments in light alloys," Mater. Trans. JIM **37**, 12–31 (1996).
[2]W. D. Brewer, R. K. Bird, and T. A. Wallace, "Titanium alloys and processing for high speed aircraft," Mater. Sci. Eng. A **243**, 299–304 (1998).
[3]R. Schutz and H. Watkins, "Recent developments in titanium alloy application in the energy industry," Mater. Sci. Eng. A **243**, 305–315 (1998).
[4]S. Sikka, Y. Vohra, and R. Chidambaram, "Omega phase in materials," Prog. Mater. Sci. **27**, 245–310 (1982).
[5]P. Frost, W. Parris, L. Hirsch, J. Doig, and C. Schwartz, "Isothermal transformation of titanium-chromium alloys," Trans. ASM **46**, 231–256 (1954).
[6]J. C. Williams, B. S. Hickman, and H. L. Marcus, "The effect of omega phase on the mechanical properties of titanium alloys," Metall. Mater. Trans. B **2**, 1913–1919 (1971).
[7]A. Kumar, C. A. Bronkhorst, and T. Lookman, "First-principles study of the α-ω phase transformation in Ti and Zr coupled to slip modes," J. Appl. Phys. **123**, 045903 (2018).
[8]F. R. Brotzen, E. L. Harmon, and A. R. Troiano, "Decomposition of beta titanium," JOM **7**, 413–419 (1955).
[9]B. Hickman, "The formation of omega phase in titanium and zirconium alloys: A review," J. Mater. Sci. **4**, 554–563 (1969).
[10]M. Tane, Y. Okuda, Y. Todaka, H. Ogi, and A. Nagakubo, "Elastic properties of single-crystalline ω phase in titanium," Acta Mater. **61**, 7543–7554 (2013).
[11]H. Zong, D. Xue, X. Ding, and T. Lookman, "Phase transformations in titanium: Anisotropic deformation of ω phase," J. Phys. **500**, 112042 (2014).
[12]Y. Todaka, J. Sasaki, T. Moto, and M. Umemoto, "Bulk submicrocrystalline ω-Ti produced by high-pressure torsion straining," Scr. Mater. **59**, 615–618 (2008).
[13]N. Adachi, Y. Todaka, K. Irie, and M. Umemoto, "Phase transformation kinetics of ω-phase in pure Ti formed by high-pressure torsion," J. Mater. Sci. **51**, 2608–2615 (2016).
[14]L. Cao and M. Koslowski, "Effect of microstructural uncertainty on the yield stress of nanocrystalline nickel," Acta Mater. **61**, 1413–1420 (2013).
[15]L. Cao, A. Hunter, I. J. Beyerlein, and M. Koslowski, "The role of partial mediated slip during quasi-static deformation of 3D nanocrystalline metals," J. Mech. Phys. Solids **78**, 415–426 (2015).
[16]A. H. Zahiri, P. Chakraborty, Y. Wang, and L. Cao, "Strong strain hardening in ultrafast melt-quenched nanocrystalline Cu: The role of fivefold twins," J. Appl. Phys. **126**, 075103 (2019).
[17]Y. Cui, P. Lin, Z. Liu, and Z. Zhuang, "Theoretical and numerical investigations of single arm dislocation source controlled plastic flow in fcc micropillars," Int. J. Plast. **55**, 279–292 (2014).
[18]J. Ombogo, A. H. Zahiri, T. Ma, and L. Cao, "Nucleation of $\{10\bar{1}2\}$ twins in magnesium through reversible martensitic phase transformation," Metals **10**, 1030 (2020).
[19]Z. Nishiyama, M. Oka, and H. Nakagawa, "$\{10\bar{1}1\}$ transformation twins in titanium," Trans. Japan Inst. Metals **7**, 174–177 (1966).
[20]C. Hammond and P. Kelly, "The crystallography of titanium alloy martensites," Acta Metallurg. **17**, 869–882 (1969).
[21]Y. Deng and Z. Qin, "Triple twins and martensitic transformation in Ti-5Al-2Mo-3Zr alloy," J. Mater. Sci. **28**, 5330–5334 (1993).
[22]S. Wang, M. Aindow, and M. Starink, "Effect of self-accommodation on α/α boundary populations in pure titanium," Acta Mater. **51**, 2485–2503 (2003).
[23]S. Plimpton, "Fast parallel algorithms for short-range molecular dynamics," J. Computat. Phys. **117**, 1–19 (1995).
[24]M. I. Mendelev, T. L. Underwood, and G. J. Ackland, "Development of an interatomic potential for the simulation of defects, plasticity, and phase transformations in titanium," J. Chem. Phys. **145**, 154102 (2016).
[25]D. J. Evans and B. L. Holian, "The Nose–Hoover thermostat," J. Chem. Phys. **83**, 4069–4074 (1985).
[26]M. Parrinello and A. Rahman, "Polymorphic transitions in single crystals: A new molecular dynamics method," J. Appl. Phys. **52**, 7182–7190 (1981).
[27]P. Chen, F. Wang, and B. Li, "Transitory phase transformations during {1012} twinning in titanium," Acta Mater. **171**, 65–78 (2019).
[28]J. Ren, Q. Sun, L. Xiao, X. Ding, and J. Sun, "Phase transformation behavior in titanium single-crystal nanopillars under [0 0 0 1] orientation tension: A molecular dynamics simulation," Comput. Mater. Sci. **92**, 8–12 (2014).
[29]L. Chang, C.-Y. Zhou, L.-L. Wen, J. Li, and X.-H. He, "Molecular dynamics study of strain rate effects on tensile behavior of single crystal titanium nanowire," Comput. Mater. Sci. **128**, 348–358 (2017).
[30]S. Rawat and N. Mitra, "Compression twinning and structural phase transformation of single crystal titanium under uniaxial compressive strain conditions: Comparison of inter-atomic potentials," Comput. Mater. Sci. **126**, 228–237 (2017).
[31]A. Stukowski, "Visualization and analysis of atomistic simulation data with OVITO—The open visualization tool," Model. Simul. Mater. Sci. Eng. **18**, 015012 (2009).
[32]D. Faken and H. Jónsson, "Systematic analysis of local atomic structure combined with 3D computer graphics," Comput. Mater. Sci **2**, 279–286 (1994).
[33]J. D. Honeycutt and H. C. Andersen, "Molecular dynamics study of melting and freezing of small Lennard-Jones clusters," J. Phys. Chem. **91**, 4950–4963 (1987).
[34]R. G. Hennig, T. J. Lenosky, D. R. Trinkle, S. P. Rudin, and J. W. Wilkins, "Classical potential describes martensitic phase transformations between the α, β, and ω titanium phases," Phys. Rev. B **78**, 054121 (2008).
[35]M. P. Usikov and V. A. Zilbershtein, "The orientation relationship between the ω-phases of titanium and zirconium," Phys. Status Solidi A **19**, 53–58 (1973).
[36]S. Wang, M. Sui, Y. Chen *et al.*, "Microstructural fingerprints of phase transitions in shock-loaded iron," Sci. Rep. **3**, 1086 (2013).
[37]D. Schryvers, "Martensitic and related transformations in Ni-Al alloys," J. Phys. IV **5**, C2-225–C2-234 (1995).
[38]M. Lai, T. Li, and D. Raabe, "ω phase acts as a switch between dislocation channeling and joint twinning-and transformation-induced plasticity in a metastable β titanium alloy," Acta Mater. **151**, 67–77 (2018).
[39]S. A. Mantri, F. Sun, D. Choudhuri, T. Alam, B. Gwalani, F. Prima, and R. Banerjee, "Deformation induced hierarchical twinning coupled with omega transformation in a metastable β-ti alloy," Sci. Rep. **9**, 1–8 (2019).
[40]D. A. Porter and K. E. Easterling, *Phase Transformations in Metals and Alloys (revised reprint)* (CRC Press, 2009).
[41]J. Silcock, "An x-ray examination of the to phase in TiV, TiMo and TiCr alloys," Acta Metallur. **6**, 481–493 (1958).
[42]Y. Vohra, S. Sikka, S. Vaidya, and R. Chidambaram, "Impurity effects and reaction kinetics of the pressure-induced α–ω transformation in Ti," J. Phys. Chem. Solids **38**, 1293–1296 (1977).
[43]Y. Vohra, S. Sikka, E. Menon, and R. Krishnan, "Direct evidence of intermediate state during alpha-omega transformation in Ti-V alloy," Acta Metallur. **28**, 683–685 (1980).
[44]H. Xia, G. Parthasarathy, H. Luo, Y. K. Vohra, and A. L. Ruoff, "Crystal structures of group iva metals at ultrahigh pressures," Phys. Rev. B **42**, 6736 (1990).
[45]S. Song and G. Gray III, "Microscopic and crystallographic aspects of retained omega phase in shock-loaded zirconium and its formation mechanism," Philos. Mag. A **71**, 275–290 (1995).
[46]D. Trinkle, R. Hennig, S. Srinivasan, D. Hatch, M. Jones, H. Stokes, R. Albers, and J. Wilkins, "New mechanism for the α to ω martensitic transformation in pure titanium," Phys. Rev. Lett. **91**, 025701 (2003).

[47]G. Jyoti, R. Tewari, K. Joshi, D. Srivastava, G. Dey, S. Gupta, S. Sikka, and S. Banerjee, "Alpha to omega transition in shock compressed zirconium: Crystallographic aspects," in *Defect and Diffusion Forum*, Vol. 279 (Trans Tech Publications, 2008), pp. 133–138.
[48]H. Zong, T. Lookman, X. Ding, S.-N. Luo, and J. Sun, "Anisotropic shock response of titanium: Reorientation and transformation mechanisms," Acta Mater. **65**, 10–18 (2014).
[49]T. Swinburne, M. Glavicic, K. Rahman, N. Jones, J. Coakley, D. Eakins, T. White, V. Tong, D. Milathianaki, and G. Williams *et al.*, "Picosecond dynamics of a shock-driven displacive phase transformation in Zr," Phys. Rev. B **93**, 144119 (2016).
[50]W. Petry, A. Heiming, J. Trampenau, M. Alba, C. Herzig, H. R. Schober, and G. Vogl, "Phonon dispersion of the bcc phase of group-IV metals. I. Bcc titanium," Phys. Rev. B **43**, 10933–10947 (1991).